Journal of Energy Storage 150 (2026) 120397

Contents lists available at ScienceDirect

Journal of Energy Storage

journal homepage: www.elsevier.com/locate/est

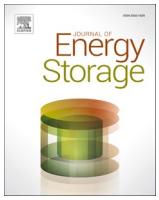

Research papers

Upcycling chrome-tanned leather waste into electrode materials for supercapacitors and high-voltage Li-ion batteries

Nikhitha Joseph [a,b], Tomáš Sáha [b], Matej Micusik [c], Petr Sáha [a,b], Haojie Fei [a,b,*]

[a] Centre of Polymer Systems, Tomas Bata University in Zlin, 760 01, Zlin, Czech Republic
[b] Footwear Research Centre, Tomas Bata University in Zlin, 760 01, Zlin, Czech Republic
[c] Polymer Institute, Slovak Academy of Sciences, Dúbravská cesta 9, 845 41, Bratislava, Slovakia

ARTICLE INFO

Keywords:
Chromium-tanned leather
Physical separation
Activated carbon
Supercapacitor
$LiMnCrO_4$
Li-ion battery

ABSTRACT

Conventional disposal methods of chromium-tanned leather waste (CTLW) pose significant environmental pollution and potential leaching of heavy metals into soil and water. To address this issue, we designed a sustainable recycling method to convert CTLW into value-added products through chromium extraction and activated carbon production. Three different approaches, including two solution-phase extractions using H_2SO_4 and NaOH, and a solid-phase physical separation using $CHCl_3$-H_2O, were introduced to remove Cr from the chemically activated biochar. The physicochemical analysis shows no trace of Cr in the final carbon sample, which is highly microporous and has a specific surface area of 1934 $m^2\ g^{-1}$. The activated carbon was then used in a symmetric supercapacitor and tested in organic and aqueous electrolytes. The cell exhibits a maximum specific capacitance of 181.4 F g^{-1} in 6 M KOH, and 112.8 F g^{-1} in 1 M $TEABF_4$/ACN electrolytes at 1 A g^{-1}. The extracted Cr in the form of Cr_2O_3 was used to produce high-voltage cathode material, $LiMnCrO_4$. The prepared Li-half cell shows a high specific capacity of 192.7 mAh g^{-1} along with notable stability and coulombic efficiency. This dual-functional approach mitigates environmental hazards and promotes sustainable resource utilization for energy storage applications.

1. Introduction

Leather manufacturing is indisputably a major industry with a significant economic impact on an international scale. The tanning process plays a significant role in leather production, improving the durability and versatility of hides and skins. Chromium(III) salts, such as chromium sulfate ($Cr(OH)SO_4$), are widely utilized in the leather tanning industry, and 80–90% of global leather is processed using the chrome tanning method. [1–3] The process of chromium tanning alters the collagen structure in animal skin, leading to the bonding of collagen subunits into crosslinks, which results in the formation of a collagen-chromium complex. This intricate structure arises from the chemical interaction involving the Cr(III) complex and the carboxyl groups present in aspartic and glutamic acids within the collagen framework. [4–6] As a result, the tanning agent reinforces the macromolecular framework of collagen in the hide, enhancing the durability of leather against environmental factors and various forms of biological degradation. In the processes of trimming, shaving, and finishing stages of leather production, a significant quantity of chromium-tanned leather waste (CTLW) is produced. [7,8] Under different environmental conditions, the residual Cr(III) from leather waste oxidizes to form toxic Cr (VI), which is carcinogenic and mutagenic to living organisms. [9] The existing methods for the disposal of CTLW comprise incineration and landfilling. This method of disposal leads to significant environmental issues, including air pollution and contamination of underground water resources. [10,11] These health and environmental concerns necessitate the development of sustainable large-scale recycling strategies for CTLW. Various approaches for managing chrome-tanned leather scraps have been documented, including the use of leather waste as a reinforcement agent, the synthesis of polymer-based composites, the recovery of collagen, and the implementation of thermal treatment processes for absorbent materials, among others. [12,13] Nonetheless, it is essential to remove the Cr from tanned leather before reuse to avert further environmental contamination.

Multiple approaches, such as alkaline and acid hydrolysis, oxidation-reduction reactions, physicochemical methods, and biological techniques, have been reported for the extraction of Cr from leather. Under a strong alkaline environment, the collagen fibers break and release Cr,

* Corresponding author at: Centre of Polymer Systems, Tomas Bata University in Zlin, 760 01, Zlin, Czech Republic.
E-mail address: haojie@utb.cz (H. Fei).

https://doi.org/10.1016/j.est.2026.120397
Received 15 October 2025; Received in revised form 19 December 2025; Accepted 4 January 2026
Available online 14 January 2026

making this approach particularly efficient for Cr extraction. [14] Simultaneously, strong acid hydrolysis using H_2SO_4 and HCl will effectively solubilize the Cr present in the tanned leather. [15,16] These conventional acid and alkaline hydrolysis approaches present challenges, including the breakdown of collagen or a notable reduction of collagen in the hydrolysate, making it difficult to reuse. [17] However, the recent report proves that the NaOH hydrolysis with potassium tartrate effectively separates Cr from the Cr-tanned leather shavings without extensive hydrolysis of collagen fibers and the possibility of reuse of the Cr-rich liquor as a retaining solution. [18] Other methods, such as the oxidation or reduction of Cr using agents like NaO_2 or $KMnO_4$, carry the risk of forming carcinogenic Cr(VI) and require careful handling. [19] An alternative way to efficiently repurpose CTLW is by producing activated carbon. Collagen contains significant amounts of carbon, oxygen, and nitrogen, which aid in the formation of highly porous, nitrogen-rich carbon with a high specific surface area. This porous carbon exhibits a wide range of applications, including its use as a catalyst in the oxidation of organic molecules, in microbial fuel cells, as a dye adsorbent, and beyond. [2,20–25] There are ongoing initiatives to utilize carbonized leather waste in energy storage applications, such as electrode material in Li-ion batteries, sulfur-host cathode for Li—S batteries, and supercapacitor electrodes. [20,26–29] The leather waste activated carbon (LWAC) used as a supercapacitor electrode material offers advantages, such as affordability, high porosity, excellent electrical conductivity, and robust chemical stability. [26] The chemical activation of LWAC facilitates the creation of microporosity within the structure, enhancing both the specific surface area and the kinetics of charge transport. Additionally, large surface area and microporosity establish ion-transport pathways that exhibit reduced resistance and minimized diffusion distances. [30–32] Consequently, carbon featuring hierarchical porous channels is considered a promising electrode material for use in electric double-layer capacitors (EDLCs). However, the existing studies did not deliberately remove Cr or other inorganic residues from the activated carbon, resulting in Cr leaching, high inactive surface content, and diminished electrochemical performance.

Cr is extensively utilized in the metallurgical sector as chromite ore, particularly in the production of stainless steel to enhance corrosion resistance. [33] CTLW serves as an essential resource for Cr, enabling its reuse in the production of ferrochrome and offering an alternative to chromite ore. On the other hand, various techniques exist for extracting Cr from CTLW and waste tanning solutions in the form of soluble chromate, including oxidation, alkaline treatment, and ultrasound removal. [17,34,35] The extracted Cr is subsequently used to create a Cr (III) sulfate tanning solution. [19] The residue from incinerated tanned leather contains Cr (III) oxide, Cr_2O_3, and is considered a suitable substrate for producing sodium chromite and high-carbon ferrochrome alloys. [36–38] Wang et al. described a two-step method that involves a leaching phase followed by an ion exchange phase to extract Cr from tanned waste, enabling the recycling of the chromium solution. [37] In electrochemical energy storage, Cr can be incorporated into high-voltage spinel-type cathode material, $LiMn_2O_4$, to replace some Mn and achieve high energy density by increasing the cell voltage to 5 V. [39–41] Li et al. reported a series of Li-Mn-Cr-O spinel-type oxide cathode materials and examined the benefit of Cr three-electron transfer ($Cr^{3+} \leftrightarrow Cr^{6+}$) during lithium insertion and extraction. [41] Nevertheless, there are no reports regarding the extraction of Cr from waste leather-derived activated carbon and its application in high-voltage cathode materials.

This study focuses on the sustainable recycling of the CTLW, sourced from Bata a.s. in Dolní Němčí, Czech Republic, which reduces the ecological footprint of tannery byproducts while enhancing their economic value. We used tanned leather waste to produce chemically activated, highly porous carbon, followed by the extraction of Cr. The final activated carbon was used in symmetric supercapacitors, and their performances were compared in organic and aqueous electrolytes. The applicability of this activated porous carbon, with a uniform microporous structure, can be extended to various fields such as catalysis and sensors. The extracted Cr, in the form of Cr_2O_3 and $Cr(OH)_3{\cdot}xH_2O$, obtained through acidic hydrolysis, physical separation, and alkaline hydrolysis, was used to synthesize high-voltage cathode materials, thereby enhancing the production of value-added products. The synthesized Cr in the form of Cr_2O_3 exhibits high purity and stability, which extends its applicability beyond electrochemical energy storage.

2. Materials and methods

Chromium-tanned blue leather waste (CTLW) was collected from Bata a.s. Dolní Němčí, Czech Republic. KOH (ACS reagent, ≥85%, pellets), NaOH (ACS reagent, ≥97.0%), Na_2SO_4 (ReagentPlus®, ≥99.0%), Chloroform ($CHCl_3$, for analysis EMSURE ACS, ISO, Reag. Ph Eur), HCl (ACS reagent, 37%), H_2SO_4 (98%, for analysis EMSURE), L-ascorbic acid (ACS reagent, ≥99%), $NH_3{\cdot}H_2O$ (28–30%, for analysis EMSURE ACS, Reag. Ph Eur), $Mn(CH_3CO_2)_2{\cdot}4H_2O$ (98%), LiOH (>98%), tetraethylammonium tetrafluoroborate ($TEABF_4$, for electrochemical analysis, ≥99.0%), 1.0 M $LiPF_6$ in PC battery electrolyte, Lithium difluoro(oxalato)borate (LiDFOB), polytetrafluoroethylene (PTFE, 60 wt% dispersion in H_2O), and *N*-Methyl-2-pyrrolidone (NMP, anhydrous, 99.5%) were all purchased from Sigma-Aldrich. Carbon black (Super P conductive, Alfa Aesar, 99 + %) and acetonitrile (ACN, 99.9%, Extra Dry) were purchased from Thermo Scientific Chemical. Polyvinylidene fluoride (PVDF) was purchased from MSE Supplies (USA).

2.1. Experimental section

Fig. 1 schematically illustrates the preparation steps of two CTLW-derived energy materials: (i) activated carbon for supercapacitor applications and (ii) high-voltage cathode materials for Li-ion batteries.

2.1.1. Carbonization and activation of CTLW

The CTLW powder was carbonized at 500 °C in an argon atmosphere inside a tubular furnace (GSL-1600×, MTI, USA) for 3 h at a heating rate of 5 °C min^{-1}. This biochar product was ground using a pestle and mortar, then mixed with KOH solution (1:1 weight ratio), and dried at 80 °C overnight. The black powder was further carbonized and activated in an argon atmosphere at 800 °C for 3 h inside the tubular furnace at a heat rate of 5 °C min^{-1}. This leather waste activated carbon (LWAC) was then mixed with 0.1 M HCl solution and filtered several times using deionized water, and the yellow solution was collected for Cr extraction. The remaining black powder was collected, dried at 80 °C for 12 h, and named as leather waste activated carbon-water washed (LWAC-WW). For the electrochemical test comparison, the CTLW was carbonized without KOH activation at 800 °C for 3 h, and the sample is named as CTLW-800.

2.1.2. Acid hydrolysis

To remove the remaining inorganic residues, especially the Cr in the LWAC-WW powder, the sample underwent acidic and alkaline hydrolysis. Initially, 10 g of the LWAC-WW was treated with 25% H_2SO_4 and continuously mixed using a magnetic stirrer for 12 h at 90 °C. After the reaction, the blue colored filtered solution was collected using vacuum filtration for further processing to extract Cr (shown in Fig. 1). The remaining black powder was then washed several times with deionized water, dried at 80 °C for 12 h, and named as LWAC-AH (acid hydrolyzed). After the acid hydrolysis and washing, the remaining material yield is reduced to 78%.

2.1.3. Physical separation

A physical separation method was used to remove Cr_2O_3 from LWAC-AH by using a $CHCl_3/H_2O$ immiscible mixture. Briefly, LWAC-AH powder was added to the mixture and shaken continuously for a few minutes. Due to the polarity difference between the materials, LWAC

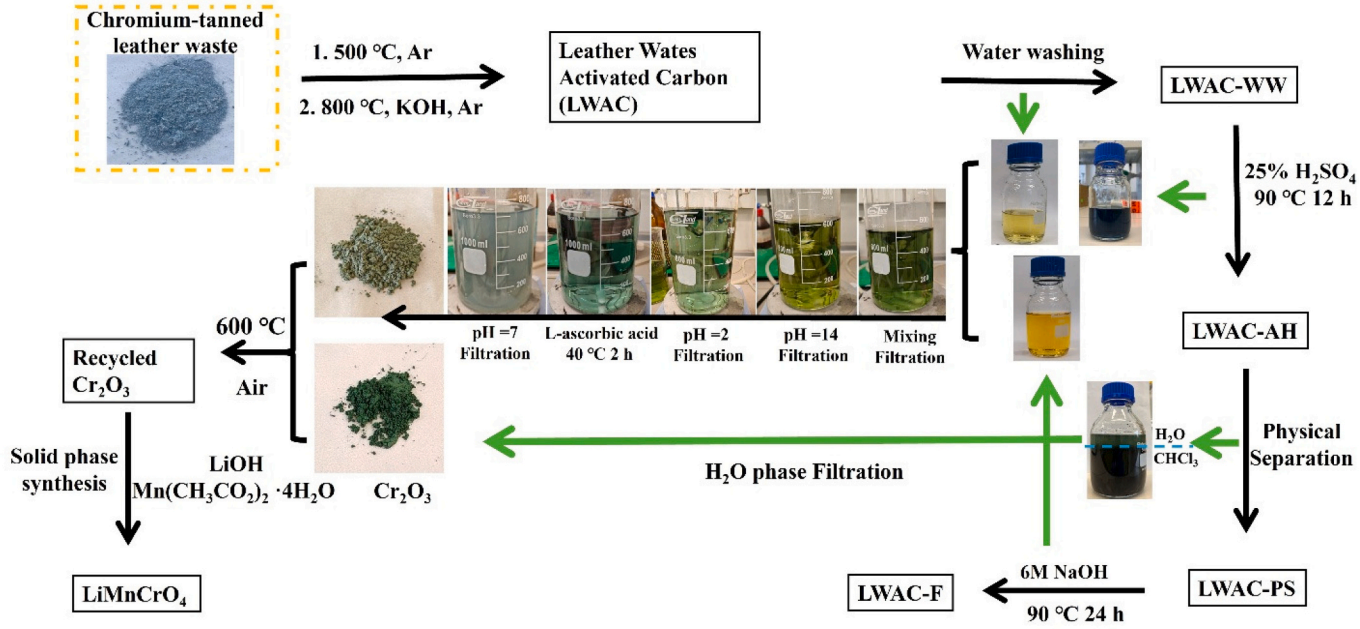

Fig. 1. Representation of the inorganic residue separation step from activated carbon and the reaction procedure for the preparation of Cr_2O_3.

particles adhered to the $CHCl_3$-water interface, while Cr_2O_3 partitioned into the water phase. The water phase was filtered, and fresh water was then added. This separation process was repeated five times until the water phase became clear. The recovered green color-Cr_2O_3 was dried at 80 °C overnight. The separated LWAC powder was further filtered, dried, and labeled as LWAC-PS (physically separated). The yield of LWAC after the physical separation method is 96%. Here, the filtered $CHCl_3/H_2O$ mixture can be easily separated using a separator funnel due to the immiscible nature of the liquids and reused for other purposes.

2.1.4. Alkaline hydrolysis

To remove the remaining Cr residues, LWAC-PS was treated with 6 M NaOH at 90 °C for 24 h. The resulting mixture was vacuum filtered, and the yellow solution was collected for the recycling of Cr. The final LWAC powder was collected and washed several times with deionized water until the pH became 7, and the sample was named as LWAC-final (LWAC-F). The yield of the LWAC sample after alkaline hydrolysis is 96%.

2.1.5. Extraction of Cr from the filtered solution

The filtered blue and yellow solutions were mixed for further Cr extraction. The mixture turned green and had a pH of 14. The pH of the solution was then adjusted to 2 by adding HCl, changing the solution color to transparent green (see Fig. 1). A mild reducing agent, L-ascorbic acid, was added to this solution at 40 °C, and the reaction continued for 2 h to reduce any Cr^{6+} in the mixture. The pH was adjusted to 7 using $NH_3{\cdot}H_2O$, and the precipitated sage green Cr-hydroxide (in Fig. 1) was filtered and dried at 80 °C overnight.

2.1.6. Preparation of $LiMnCrO_4$ for high-voltage battery cathode

The prepared Cr-hydroxide and physically separated Cr_2O_3 were mixed using a pestle and mortar and calcinated at 600 °C in air for 3 h. $LiMnCrO_4$ was prepared through a two-step calcination. Initially, the precursors 0.01 M recycled Cr_2O_3, 0.01 M $Mn(CH_3COO)_2{\cdot}4H_2O$, and 0.01 M LiOH (5% in molar ratio excess) were mixed using a pestle and mortar by adding a few drops of deionized water. This mixture was dried at 80 °C, and the dried powder was ground again and calcinated at 450 °C for 5 h in air. The resulting powder was collected, ground, and further calcinated at 850 °C for 10 h in air to obtain the final product.

2.2. Characterization

The X-ray diffraction (XRD) analysis of the activated carbon and other samples was recorded on a Rigaku MiniFlex 600 diffractometer equipped with a CoKα (k = 1.7903 Å) radiation in a range from 5° to 120° at a scan rate of 5° min^{-1}. The thermal degradation of the prepared samples was estimated using thermogravimetric analysis (TGA, TA Q500, TA Instruments, USA), carried out under an air atmosphere (100 mL min^{-1}) from 25 to 700 °C with a heat rate of 10 °C min^{-1}. The morphology and elemental analysis of the prepared samples were confirmed by scanning electron microscopy (SEM) using Nova Nano SEM 450 (FEI, USA), together with an energy-dispersive X-ray detector (EDX). X-ray photoelectron spectroscopy studies (XPS) were conducted using NEXSA-G2, a monochromated high-performance XPS spectrometer (Thermo Scientific, UK), to examine the Cr residues, chemical composition, and binding energy of the prepared samples. The nitrogen adsorption/desorption isotherms were obtained using BELSORP-mini II volumetric sorption surface area and porosity analyzer.

2.2.1. Electrochemical characterization

2.2.1.1. Supercapacitor cell assembly and testing. The supercapacitor electrodes were prepared by mixing the LWAC-F sample (80 wt% of active material) with 10 wt% of carbon black and 10 wt% of PTFE with a pestle in an agate mortar. The resulting mixture was pressed and rolled to obtain a film. Its thickness was modulated to obtain the desired electrode mass loading. Finally, the film was cut into discs with a diameter of 8 mm and 0.16 mm thickness and pressed onto stainless-steel meshes. The average mass loading of the working electrode is 9.3 mg cm^{-2}. The electrochemical performance of the prepared LWAC-F working electrodes was initially investigated using an Ag/AgCl reference and a platinum wire counter electrode system. For comparison, CTLW-800 and LWAC-WW electrodes were prepared in the same method. The cyclic voltammetry (CV) and galvanostatic charge/discharge (GCD) analysis were carried out in 6 M KOH electrolyte using an Autolab PGSTAT 128 N potentiostat (Metrohm, Prague, Czech Republic). The symmetric cells using aqueous solutions of 6 M KOH, 1 M Na_2SO_4, and 1 M H_2SO_4 were assembled in a Swagelok cell using cellulose separators. The symmetric cells with 1 M $TEABF_4$/ACN organic electrolyte were assembled using LWAC-F free-standing films with a

diameter of 12 mm and a thickness of 0.16 mm in coin cells (CR2032). The electrochemical performance of the symmetric cells was carried out using an Autolab PGSTAT 128 N potentiostat and a BCS-810 battery cycler (BioLogic, Seyssinet-Pariset, France).

2.2.1.2. Li-ion coin cell assembly. The electrochemical testing of high-voltage $LiMnCrO_4$ was conducted using CR2023 coin cells. Briefly, the working electrode was prepared by mixing the $LiMnCrO_4$ active materials, conductive carbon black, and PVDF in a mass ratio of 8:1:1 dissolved in NMP to form a slurry. Subsequently, the prepared slurry was evenly coated on Al foil using the doctor blade method and dried in a vacuum at 120 °C for 12 h. The dried electrode sheet was cold pressed using a rolling machine and cut into a circular shape with a 14 mm diameter and 0.15 mm thickness. The mass of the electrode material is 2.5 mg cm^{-2}. The coin cells were assembled in an Ar-filled glovebox with Li-metal as counter electrode and reference electrode, 1 M $LiPF_6$ in PC as an electrolyte (called the BASE electrolyte), and 1% LiDFOB added BASE electrolyte using Whatman GF/A as a separator. The half-cells were analyzed using cyclic voltammetry (CV) and galvanostatic charge-discharge (GCD) techniques in two different voltage ranges of 2.0 to 4.95 V and 3.5 to 4.95 V, using a Bio-Logic BCS-810 battery cycler at room temperature.

3. Results and discussion

3.1. Cr extraction mechanism and recycling method of CTLW

By integrating experimental observations (shown in Fig. 1) with comprehensive characterization data, we elucidate the Cr extraction mechanism and demonstrate an efficient CTLW recycling strategy. Fig. 2 presents the structural and compositional evolution of CTLW throughout the purification process, highlighting the significant chemical reactions involved. During the tanning of leather using Cr (III) salt, Cr coordinates with the carboxylic groups of aspartic and glutamic acids, and the collagen molecule is expected to function as a compact ligand, maintaining its tertiary structure upon coordination. The Cr-bridging is predominantly intermolecular rather than intramolecular, and at the final stage of tanning, the stability of the collagen fibers is enhanced through the formation of hydroxyl (OH) bridges between neighboring Cr(III) complexes. At 500 °C in an Ar atmosphere, collagen fibers undergo decomposition and carbonization, forming a solid carbonaceous residue known as biochar, while the Cr complex bridge experiences dehydration. Consequently, the CTLW transforms into a composite of biochar and dehydrated chromium organic complexes (C/D-Cr-OC), as illustrated in Reaction 1. The formation of Cr inorganics does not occur at this temperature, as Cr continues to be strongly coordinated with the nitrogen and oxygen functional groups found in biochar. The C/D-Cr-OC undergoes treatment with KOH at 800 °C to improve carbonization and graphitization while completing the chemical activation of the biochar, leading to the formation of LWAC (Reaction 2). Concurrently, the D-Cr-OC undergoes decomposition and crystallization, leading to the formation of Cr_2O_3. Most of the Cr_2O_3 likely adheres to the surface of activated carbon because of concentration gradients during the tanning process. Nonetheless, the reducing environment established by pyrolysis gases (including CO and H_2) along with the carbon leads to the partial reduction of Cr_2O_3 to CrO (Reaction 3). CrO is expected to form at the interface between Cr_2O_3 and activated carbon, as shown in the composition diagram of LWAC-WW (Fig. 2). In the process of acid hydrolysis, CrO interacts with H_2SO_4 (Reaction 4), leading to the dissolution of Cr^{2+} in the solution, which exhibits a blue color (pH < 7), as shown in Fig. 1 (acid hydrolysis). However, Cr_2O_3 becomes unable to react with H_2SO_4. Due to the removal of the CrO interface, Cr_2O_3 detaches from the carbon surface, as shown in supplementary information (SI) Fig. S1 and the composition diagram of LWAC-AH in Fig. 2. Consequently, Cr_2O_3 can be separated physically using $CHCl_3$-H_2O because of the difference in polarity between the materials. The LWAC particles adhere to the $CHCl_3$-H_2O interface, while Cr_2O_3 moves into the water phase, as shown in Fig. 3(a)&(b). The separated Cr_2O_3-water mixture and Carbon-$CHCl_3$-H_2O are displayed in Fig. 3(c)&(d), respectively. A detailed video illustrating the physical separation method is provided in SI video 1. This physical separation can reduce the formation of hazardous Cr(VI) during alkaline hydrolysis while enhancing the removal of Cr_2O_3, which typically reacts at a slower rate due to its stability. Considering the physical characteristics of Cr_2O_3 and activated carbon, including variations in density, different separation techniques like centrifugation may be employed.

Fig. 3(e) illustrates the Cr_2O_3 that is isolated from the carbon skeleton via centrifugation. The LWAC-PS sample is subjected to further hydrolysis in an alkaline environment with 6 M NaOH to ensure the complete removal of Cr_2O_3 from the LWAC. This hydrolysis process leads to the oxidation of Cr_2O_3 (Reaction 5). The Cr^{6+} becomes CrO_4^{2-} in NaOH solution with a pH of 14, resulting in a dark yellow color as shown in Fig. 1 (alkaline hydrolysis). After the alkaline hydrolysis process, the Cr is completely extracted from the LWAC. This final sample (LWAC-F) is used as a suitable electrode material for supercapacitors. The filtered yellow (CrO_4^{2-}) and blue (Cr^{2+}) solutions were combined to recycle the Cr, resulting in a color change to green $[Cr(OH)_4]^-$ (Fig. 1) due to the reaction between CrO_4^{2-} and Cr^{2+} (Reaction 6). To achieve a complete reduction of hazardous Cr(VI), L-ascorbic acid is used as a reducing agent, as shown in Reaction 7, where Cr^{6+} is generally present as $Cr_2O_7^{2-}$ in acidic solution. $Cr(OH)_3{\cdot}xH_2O$ is precipitated in the solution (pH ~ 7) as shown in Reaction 8. The obtained $Cr(OH)_3.xH_2O$ was subsequently subjected to calcination at 600 °C to produce Cr_2O_3, which is then used for the preparation of battery cathode material, $LiMnCrO_4$.

3.2. Physicochemical analysis

Fig. 4(a) displays the XRD patterns for the prepared CTLW, LWAC-WW, LWAC-AH, and LWAC-F samples. The distinct diffraction peaks observed at 20° and 45° indicate the presence of carbon in the samples. Minor peaks noted between 25° and 30° in the CTLW sample result from impurities during leather production, which are eliminated after activation and water washing. Following the chemical activation, diffraction peaks were noted at 21.12°, 29.29°, 37.04°, and 45.03°, identified as the presence of $KAlSiO_4$. During the activation process, KOH reacts with the Al and Si impurities present in the tanned leather, initiating the formation of $KAlSiO_4$. This indicates that the impurity in CTLW is associated with compounds of Al and Si, including silica and alumina. The minor diffraction peaks observed at 24.7°, 34.1°, 36.8°, 41.5°, and 58.24° in the LWAC-WW sample show the presence of Cr_2O_3. An additional diffraction peak at 35.4° indicates the existence of CrO, due to the reduction of Cr_2O_3. Following the acid hydrolysis, the peak corresponding to $KAlSiO_4$ disappeared, but minor diffraction peaks representing Cr_2O_3 are still present. The XRD pattern of the LWAC-PS shows no peaks corresponding to Cr_2O_3, confirming that Cr_2O_3 was successfully removed from the LWAC-AH through the physical separation method. The XRD pattern of LWAC-F after alkaline hydrolysis does not show any peaks representing Cr_2O_3 or CrO, confirming that the sample is pure carbon, as further verified by TGA and XPS analysis.

The nitrogen adsorption-desorption isotherm analysis was performed to determine the surface area and pore size distribution. All the prepared samples exhibit a type 1 isotherm characterized by a rise and plateau at high relative pressures (P/P_0), as provided in Fig. 4(b). This type of isotherm suggests that the sample contains micropores with a pore diameter less than 2 nm. Our prior investigation demonstrates that KOH chemical activation markedly increases the specific surface area of the material. [42] The alkaline hydrolyzed final carbonized sample, LWAC-F, shows a specific surface area (S_{BET}) of 1934 $m^2\ g^{-1}$. The surface areas measured for LWAC-WW, LWAC-AH, and LWAC-PS samples are 1383 $m^2\ g^{-1}$, 1814 $m^2\ g^{-1}$, and 1836 $m^2\ g^{-1}$, respectively. The S_{BET} of the samples increases after hydrolysis due to the significant extraction of

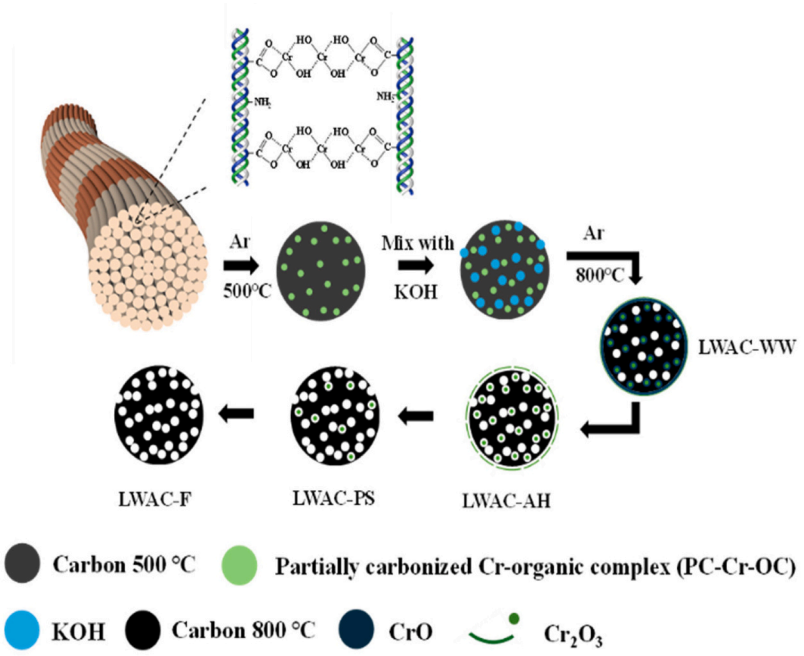

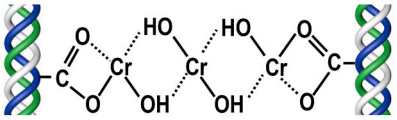

$$\xrightarrow{500\ ^\circ C} \text{C/(D-Cr-OC)} \quad (1)$$

$$\text{C/(D-Cr-OC)} + \text{KOH} \xrightarrow{800\ ^\circ C} \text{C(activated)} + Cr_2O_3 + CO_2 + CO + H_2 \quad (2)$$

$$Cr_2O_3\,(\text{partial}) + C + CO + H_2 \xrightarrow{800\ ^\circ C} CrO + CO_2 + H_2O \quad (3)$$

$$CrO\,(s) + H^+ \xrightarrow{90\ ^\circ C} Cr^{2+} + H_2O \quad (4)$$

$$Cr_2O_3\,(s) + OH^- + O_2 \xrightarrow{90\ ^\circ C} CrO_4^{2-} + H_2O \quad (5)$$

$$Cr^{2+} + CrO_4^{2-} + OH^- \xrightarrow{pH\sim14} [Cr(OH)_4]^- \quad (6)$$

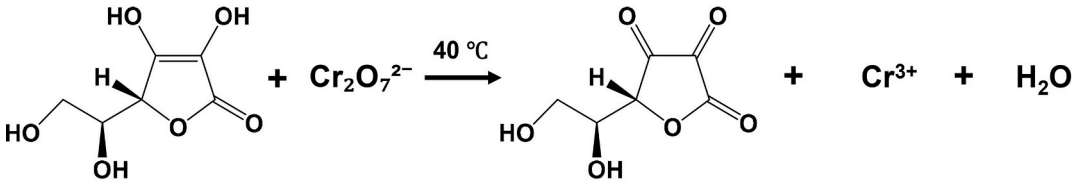

$$+ Cr_2O_7^{2-} \xrightarrow{40\ ^\circ C}$$

$$+ Cr^{3+} + H_2O \quad (7)$$

$$Cr^{3+} + OH^- \xrightarrow{pH\sim7} Cr(OH)_3 \downarrow \quad (8)$$

Fig. 2. Presents the structural and compositional evolution of CTLW throughout the purification process, along with the key associated chemical reactions.

Cr_2O_3 and CrO and the removal of other inorganic residues from the LWAC-WW. The pore size distribution of the samples is shown in the supporting information, Fig. S2, and the average pore diameter is calculated using BJH analysis. There is no difference observed in the pore size distribution of the samples, indicating that the proposed Cr removal methods do not affect the physical characteristics of the samples. The BET specific surface area, BJH pore volume, and r_p (area) results are provided in SI Table S1.

Thermogravimetry analysis was conducted to confirm the weight loss of LWAC samples after each chemical and physical reaction step. The thermograms of the prepared samples are provided in Fig. 4(c), excluding the absorbed water loss (< 120 °C). A significant weight reduction of 72% was noted in the LWAC-WW sample up to 400 °C, attributed to the combustion of carbon in the air atmosphere. There was no notable weight loss after 430 °C, leaving an inorganic residue of 28 wt%, which includes Al, K, Si, and Cr. The LWAC-AH exhibits a weight

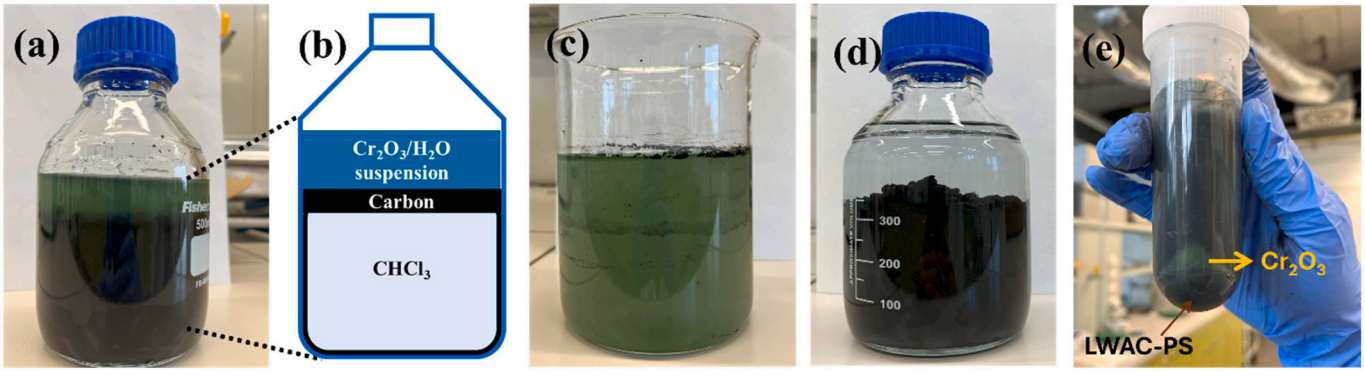

Fig. 3. (a)&(b) Physically separated Cr_2O_3 and LWAC in $CHCl_3/H_2O$ solution and their illustration, respectively, (c) Cr_2O_3 in H_2O solution, (d) LWAC-PS in $CHCl_3/H_2O$ solution, and (e) Cr_2O_3 and LWAC-PS after centrifugation in H_2O.

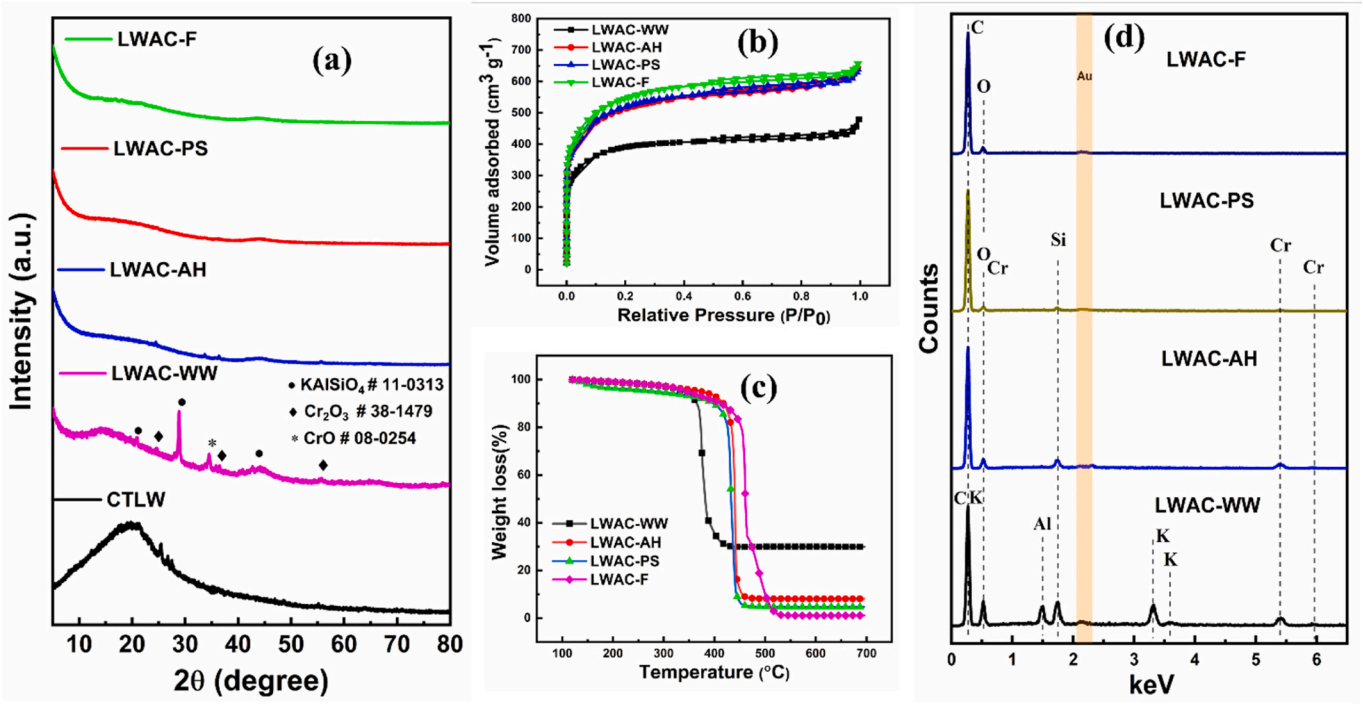

Fig. 4. Physicochemical analysis of LWAC samples. (a) XRD pattern for the prepared CTLW and LWAC samples, (b) BET surface area analysis, (c) TGA thermograms for the LWAC samples, and (d) SEM-EDX spectra for the LWAC samples.

loss of 91.4% starting at 348 °C and remains stable at 475 °C with 8.09 wt% inorganics or Cr residues. After the physical separation of Cr_2O_3, the LWAC-PS sample shows a weight loss that begins at 375 °C and stabilizes at 475 °C with a remaining 4.8% Cr residue. In the LWAC-F sample, the thermal decomposition begins at 350 °C, losing 99.11% of its weight by 530 °C, with 0.89 wt% inorganic residues remaining as ash. The analysis reveals that Cr and other inorganic impurities were progressively eliminated throughout each phase of hydrolysis and separation. Table S2 illustrates activated carbon weight loss and inorganic residue balance in the sample after each reaction process.

The SEM-EDX spectroscopy analysis was performed to verify the extraction of Cr and other inorganic residues, as well as to confirm the presence of elements on the surface of LWAC samples. The results of the SEM-EDX spectra for all the samples are illustrated in Fig. 4(d). The EDX spectrum of the LWAC-WW sample displays residual peaks, such as Cr, K, Si, and Al, in addition to carbon, which aligns with the XRD results. Followed by acid hydrolysis, Al and K are washed out from the carbon skeleton, leaving Cr and Si behind. The LWAC-PS sample exhibits similar residues as seen in LWAC-AH, even at a reduced percentage. The physical separation method effectively removes Cr_2O_3 from the surface of activated carbon, while the Cr_2O_3 particles, which are trapped within the pores, continue to remain. These trapped Cr_2O_3 cannot be washed out through a simple physical separation process. Following alkaline hydrolysis, the spectra show no residual peaks, indicating only the presence of C and O in the structure. The presence of elements on the LWAC surface is further clarified with SEM-EDX elemental mapping shown in Fig. 5 and Fig. S3. The mapping results of LWAC-WW (Fig. 5 (a)-(g)) revealed a significant distribution of chromium and aluminum on the surface, with potassium and silicon throughout the entire scan region. Fig. S3(a)-(e) presents the mapping results of LWAC-AH samples, indicating the presence of Si and Cr along with C and O. After the physical separation of Cr_2O_3, only trace amounts of Cr and Si are observed on the surface of the sample, as shown in Fig. S3(f)-(j). However, the mapping results of LWAC-F (Fig. 5(h)-(k)) indicate a notable elimination of residue elements along with a minimal presence of Si, which remains undetectable in the EDX elemental analysis due to the low trace level of the element. Consequently, the inorganic ash content in the TGA thermogram of the LWAC-F sample was mainly attributed to

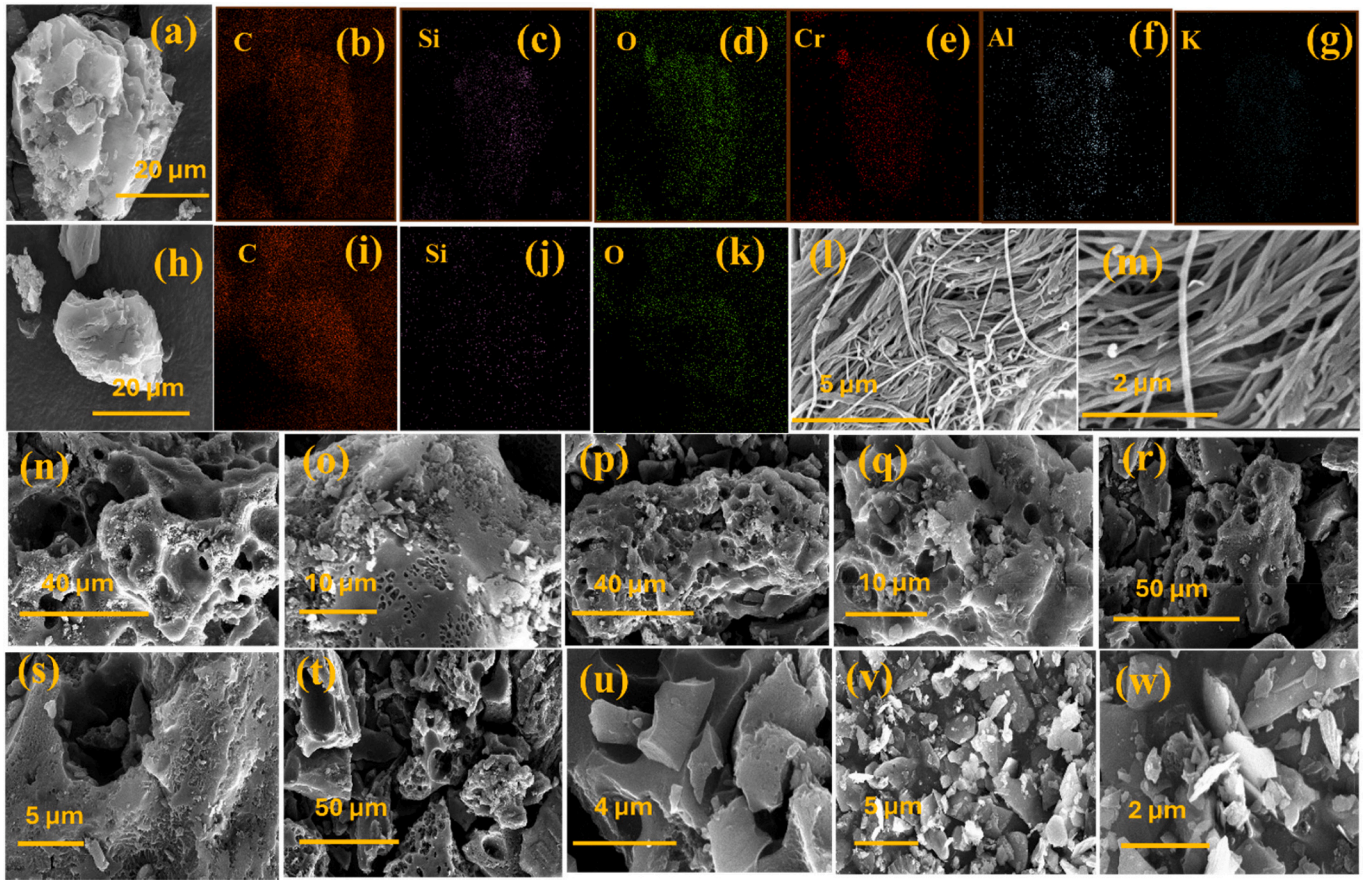

Fig. 5. SEM-EDX elemental mapping for (a-g) LWAC-WW sample, (h-k) LWAC-F, SEM images of (l-m) CTLW, (n-o) LWAC-WW, (p-q) LWAC-AH, (r-s) LWAC-PS, (t-u) LWAC-F, and (v-w) Cr_2O_3 physically separated.

the Si residue.

The surface morphology of the samples was analyzed using SEM, and the results are presented in Fig. 5. The CTLW contained well-packed collagen-fibrous tissues, shown in Fig. 5(l)&(m). After carbonization and activation with KOH, the fibrous structure collapsed, fused, and pores were formed on the surface of the carbon skeleton, as shown in Fig. 5(n)&(o). The SEM images of LWAC-WW samples (in Fig. 5(n)&(o)) reveal significant pits and voids on the surface, attributed to the interaction between carbon and KOH. The interaction between metallic K and carbon leads to gasification and pore formation within the carbon structure. Generally, the micro- and mesopores created during KOH activation at elevated temperatures are prone to merging due to the breakdown of carbon walls. This leads to the formation of macropores. Here, the presence of Cr_2O_3 on the carbon surface (detailed in Fig. S1(a)) contributes to structure stabilization and maintains the microporous characteristics of the LWAC. Small, flake-like inorganic residues that accumulate on the carbon surface after carbonization and activation at 800 °C cannot be removed through simple water washing. A detailed SEM image of the inorganic particles on the surface of LWAC-WW is provided in Fig. S1(b)&(c). From the SEM images of the LWAC-AH sample (Fig. 5(p)&(q)), the presence of aggregated flake-like structures on the surface of the carbon skeleton is significantly reduced compared to the LWAC-WW sample. The morphology of the LWAC-PS samples is provided in Fig. 5(r)&(s), revealing a similar structure to that of LWAC-WW and LWAC-AH. A negligible percentage of flaky particles on the surface indicates that most of the Cr and Si are washed out from the carbon surface. The etched-like surface morphology of the LWAC-PS sample (shown in Fig. S1(d)) arises from the physical separation of Cr_2O_3 and exposure of the inner surface of carbon due to the reaction between CrO and H_2SO_4. The morphology of the LWAC-F sample is illustrated in Fig. 5(t)&(u). This final sample exhibits no morphological differences compared to the others, and the high-magnification SEM image verifies that there are no aggregated inorganic structures present on the surface (Fig. 5(t)). The morphology of the physically separated flake-like Cr_2O_3 from the carbon skeleton is shown in Fig. 5(u)&(v), revealing a flake-like non-aggregated particle structure.

Fig. 6(a) presents the XPS survey spectra for the LWAC-WW and LWAC-F samples. The prominent peaks of C1s, Cr2p, and O1s were detected in the LWAC-WW sample, in addition to N1s and S2s peaks. Notably, the XPS spectrum of the LWAC-WW sample contains minor impurity peaks corresponding to Si, Al, K, and Cr, which are absent in the LWAC-F spectrum. A new peak was observed in the LWAC-F sample spectrum at 537.2 eV, which signifies the Auger electron peak for Na KL1, due to the alkaline hydrolysis. The comprehensive spectrum for C1s, O1s, N1s, Si2p, and Al2s in the LWAC-WW sample is provided in Fig. 6(b)&(c). The C1s spectrum displays multiple peaks, C—C (284.4 eV and 284.8 eV), C—O (286.0 eV), C═O (287.2 eV), NC═O (288.3 eV), and O-C═O (289.9 eV), corresponding to graphitic carbon, hydroxyl, carbonyl, and carboxyl groups, respectively. The increase in oxygenated carbon groups is attributed to the oxidative chemical activation method, and similar behavior is observed in the C1s spectrum of the LWAC-F sample (Fig. 6(d)). The Cr2p state in the LWAC-WW sample was validated by the peaks observed at 577.2 eV ($Cr2p_{3/2}$) and 587.0 eV ($Cr2p_{1/2}$), as shown in Fig. 6(b). The intensity of the Si2p spectrum shows a significant reduction in the LWAC-F sample compared to LWAC-WW. The atomic percentages for each element in both samples can be found in Table S3 in the SI.

Fig. 7(a) illustrates the XRD pattern of the physically separated Cr from the LWAC-PS using $CHCl_3/H_2O$ solution. The (hkl) planes

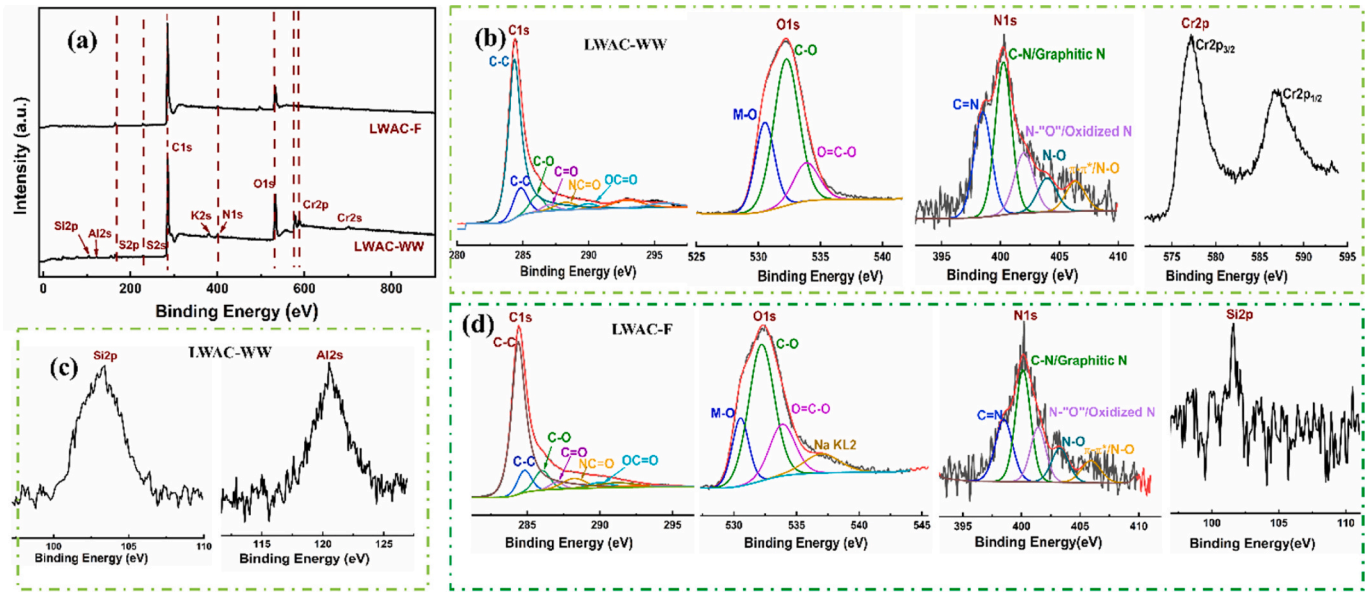

Fig. 6. (a) XPS survey spectra for LWAC-WW and LWAC-F samples, (b) deconvoluted spectrum of C1s, O1s, N1s, and Cr2p state in LWAC-WW sample, (c) Si2p and Al2s states in LWAC-WW, and (d) deconvoluted C1s, O1s, N1s, and Si2p state in LWAC-F sample.

correspond to Cr_2O_3, characterized by the rhombohedral Bravais lattice belonging to the R-3c space group. The additional signals at 30.3°, 36.0°, 44.05°, and 58.6° further validate the existence of CrO in the sample. As provided in Fig. S4, the XRD pattern of the Cr extracted from the vacuum-filtered solution is identified as $Cr(OH)_3.xH_2O$. Following calcination at 600 °C in air, the extracted $Cr(OH)_3.xH_2O$ and the physically separated Cr_2O_3-CrO undergo a complete transformation into Cr_2O_3. The Rietveld refined XRD pattern of the calcinated Cr_2O_3 is presented in Fig. 7(b), confirming that there is no trace of CrO remains in the sample. The composition and structure of the prepared $LiMnCrO_4$ were analyzed through Rietveld refinement powder diffraction data using Co-$_{K\alpha}$ source, and the result is shown in Fig. 7(c). This pattern of the $LiMnCrO_4$ spinel-derived structure is classified within the orthorhombic crystal system. All the (hkl) planes validate the presence of $LiMnCrO_4$, showing no signs of impurity peaks or secondary phases in the refined pattern.

The morphology of the Cr_2O_3 particles obtained through calcination of Cr-precipitate at 600 °C is shown in Fig. 7(d), confirming that the Cr_2O_3 consists of aggregated nanoparticles. SEM images of the prepared $LiMnCrO_4$ are presented in Fig. 7(e)&(f), revealing uniform primary particles with an average size of 200 nm. These nanosized particles are beneficial for enhancing the lithium diffusion during the high-rate performance of $LiMnCrO_4$ as a battery cathode material. The SEM images reveal a typical spinel phase morphology with a truncated octahedral grain along with (111) faceted planes of $LiMnCrO_4$. In the inset of Fig. 7 (f), the diagram of a standard truncated octahedron is presented for comparison. The XPS survey spectrum for the $LiMnCrO_4$ sample is provided in Fig. 7(g), highlighting the peaks that signify the presence of Mn2s, Mn2p, Cr2s, Cr2p, and O1s states. The binding energy values of 642.6 eV and 654.5 eV, shown in Fig. 7(h), are associated with the $Mn2p_{3/2}$ and $Mn2p_{1/2}$ states, respectively. The Cr2p spectrum shows two peaks representing $Cr2p_{3/2}$ and $Cr2p_{1/2}$ at 576.0 eV and 585.9 eV, respectively (in Fig. 7(h)). The deconvoluted O1s spectrum reveals a prominent metal-oxygen bond at 529.7 eV, an oxygen vacancy at 531.5 eV resulting from high-temperature calcination, along with a hydroxyl bond C—O at 532.6 eV. Table S2 presents the atomic percentages of each element derived from the XPS analysis.

3.3. *Electrochemical charge storage behavior of LWAC-F*

Three distinct electrodes were prepared with CTLW-800, LWAC-WW, and LWAC-F and tested in a 6 M KOH using a three-electrode setup to assess the impact of KOH activation and the removal of inorganic residues on electrochemical performance. Fig. 8(a) illustrates the CV performance of the CTLW-800, LWAC-WW, and LWAC-F electrodes at 5 mV s^{-1} scan rate. The current response of the LWAC-F within the potential range of −1.1 to −0.1 V is significantly higher compared to that of CTLW-800 and LWAC-WW. The CV curve of LWAC-F at various scan rates is provided in Fig. 8(b), and for the CTLW and LWAC-WW electrodes are shown in Fig. S5(a)&(b), respectively. As the scan rate increases, the rectangular CV shape of the CTLW-800 electrode becomes distorted, pointing out that the material is losing its capacitive behavior. Compared to the CTLW-800, the LWAC-WW and LWAC-F electrodes show a better CV performance and rate capability at scan rates above 50 mV s^{-1}. Here, the KOH activation introduces oxygenated surface functional groups and enhances the wettability of the LWAC-F and LWAC-WW electrode surfaces. The presence of these oxygenated functional groups enhances the pseudocapacitance, and electrodes with KOH activation will have improved rate performance. Additionally, removing unwanted inorganic residues like Al, K, Cr, and Si from the carbon structure helps enhance electrochemical performance. Consequently, to optimize the utilization of the LWAC from the CTLW for energy storage applications, it is strongly advised to remove the inorganic residues. In addition to this, Cr compounds can be oxidized at high potential in KOH and released into the electrolyte, as shown in Fig. S7(a)-(c). Due to the toxicity of high valence Cr, aqueous supercapacitors using the LWAC with Cr residue require careful recycling, emphasizing the importance of the upcycling method presented in this study.

The charge-discharge performance of the electrodes at 0.5 A g^{-1} is illustrated in Fig. 8(c). The LWAC-F electrode exhibits the maximum specific capacitance of 205 F g^{-1} at 0.5 A g^{-1}. The charge-discharge performances of CTLW-800, LWAC-WW, and LWAC-F at different current densities are plotted in Fig. 8(d) and Fig. S5(c)&(d), respectively. The observed voltage drop with current density is higher for CTLW and LWAC-WW electrodes than for LWAC-F. This IR drop shows an increased electrode resistance with current density. Fig. 8(e) presents the rate performance of the electrodes, where the LWAC-F electrode maintains the highest capacitance retention of 84% at 15 A g^{-1}. Conversely, the capacitance retention for CTLW-800 and LWAC-WW electrodes is 40% and 72.4% at 10 A g^{-1} and 15 A g^{-1} current densities, respectively. From the Nyquist plot given in Fig. 8(f), the initial x-intercept signifies the solution resistance (R_S), which is reduced for the LWAC-F, compared to

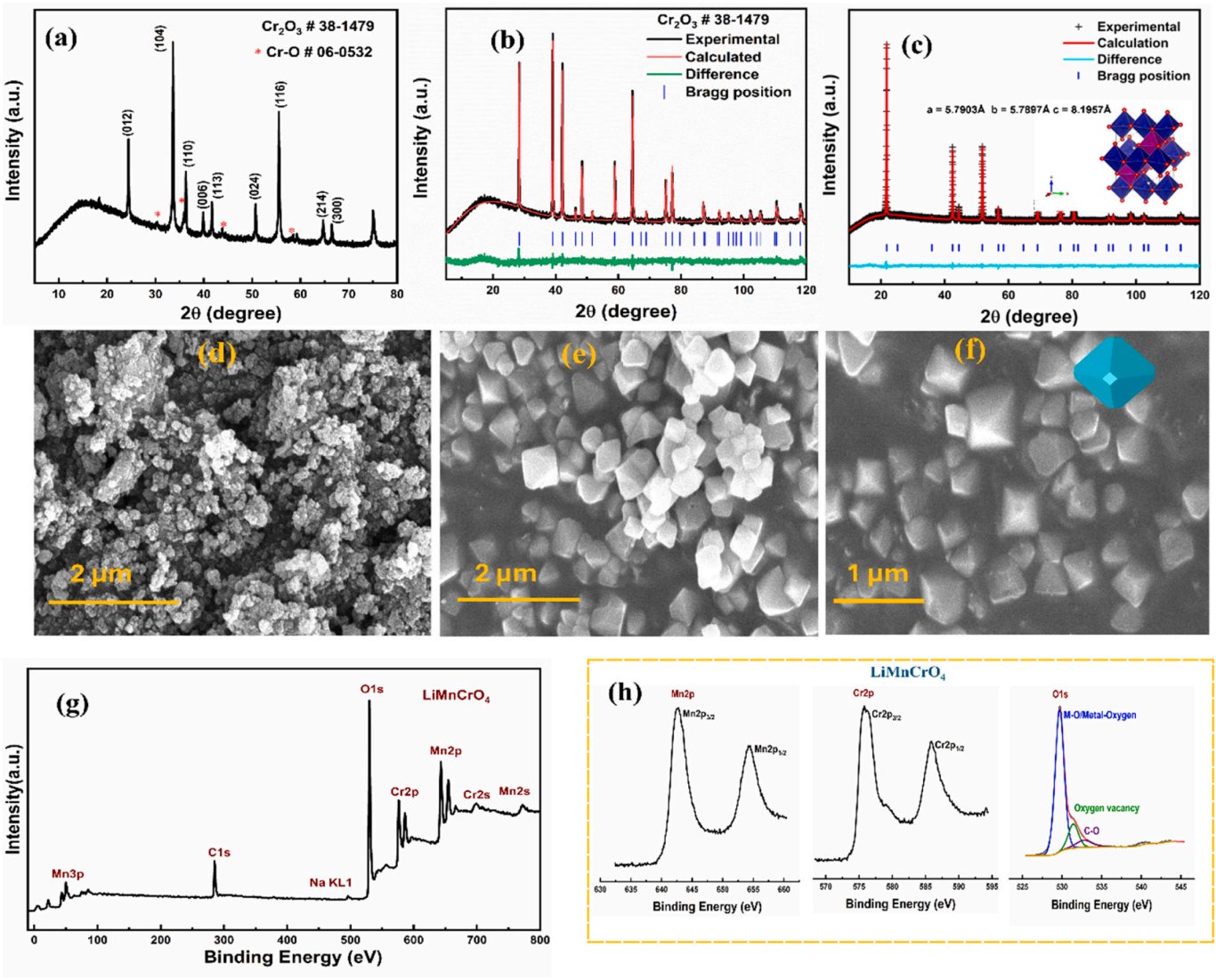

Fig. 7. (a) Powder XRD pattern for the physically separated Cr_2O_3 particles, (b) Rietveld refined powder XRD pattern for Cr_2O_3 calcinated at 600 °C, (c) refined XRD pattern for the $LiMnCrO_4$ cathode material, (d) SEM morphology of the physically separated Cr_2O_3, and (e)&(f) $LiMnCrO_4$ particles, and (g)&(h) XPS survey spectrum for the $LiMnCrO_4$ and spectrum for Mn2p, Cr2p and O1s, respectively.

that of LWAC-WW and CTLW-800 electrodes (the high-frequency regions provided in the inset Fig. 8(f)). Here, CTLW-800 and LWAC-WW electrodes show similar charge transfer resistance (R_{ct}) and diffusion characteristics. However, the LWAC-F electrode exhibits a reduced R_{ct} value and enhanced capacitive characteristics, indicated by the linear response observed in the high-frequency domain. This suggests that the LWAC-F electrode material possesses an enhanced ionic conductivity due to the removal of inorganic residues.

Symmetric cells were fabricated using LWAC-F, and their performances were evaluated in 1 M H_2SO_4, 6 M KOH, 1 M Na_2SO_4, and 1 M $TEABF_4$/ACN electrolytes. Fig. 9(a) presents the CV performances of the cells at 20 mV s^{-1} scan rate in the aqueous electrolytes. The cell exhibits an increased current response and a well-defined rectangular curve in KOH electrolyte compared to others. Furthermore, the rectangular CV behavior is maintained at a high scan rate of 200 mV s^{-1} (shown in Fig. S7(a)), indicating reduced charge transport resistance in 1 M KOH electrolyte. From the CV profile of the symmetric cell in 1 M Na_2SO_4 provided in Fig. S7(b), the cell cannot sustain its capacitive behavior even at a lower scan rate of 50 mV s^{-1}, due to the larger hydrated ion radius and the low ionic conductivity of Na_2SO_4 electrolyte. The CV performance of the cell in 1 M H_2SO_4 and 1 M $TEABF_4$/ACN is provided in Fig. S7(c)&(d), respectively. During the lower potential scan, the cells maintain an equilibrium rectangular shape in both electrolytes, and as the scan rate increases, the CV profile deviates from its rectangular shape. Compared to the 1 M H_2SO_4 electrolyte, the cell becomes more resistive even at 50 mV s^{-1} in the 1 M $TEABF_4$/ACN electrolyte due to the larger ionic radii of the organic electrolyte ions. The charge-discharge performance of the LWAC-F cell at various current densities in different electrolytes is illustrated in Fig. S7(e)-(h). The charge-discharge profile of the cell in 1 M Na_2SO_4 exhibits a more pronounced voltage drop at a lower current density when compared to other electrolytes.

The charge-discharge performance of the symmetric cell at 1 A g^{-1} current density in aqueous electrolytes and the specific capacitance as a function of the current density in various electrolytes are provided in Fig. 9(b)&(c), respectively. In 1 M Na_2SO_4 electrolyte, the LWAC-F symmetric cell achieves a specific capacitance of 94.54 F g^{-1} at 0.5 A g^{-1} and maintains 13.7% of its capacitance at 5 A g^{-1}. The cell has a specific capacitance of 148.0 F g^{-1}, 112.8 F g^{-1} in 1 M H_2SO_4, and 1 M $TEABF_4$/ACN electrolytes at 1 A g^{-1} and retains 51.4% and 32.7% of its capacitance at 10 A g^{-1}, respectively. The cell exhibits the highest specific capacitance of 181.4 F g^{-1} at 1 A g^{-1} in 6 M KOH electrolyte and

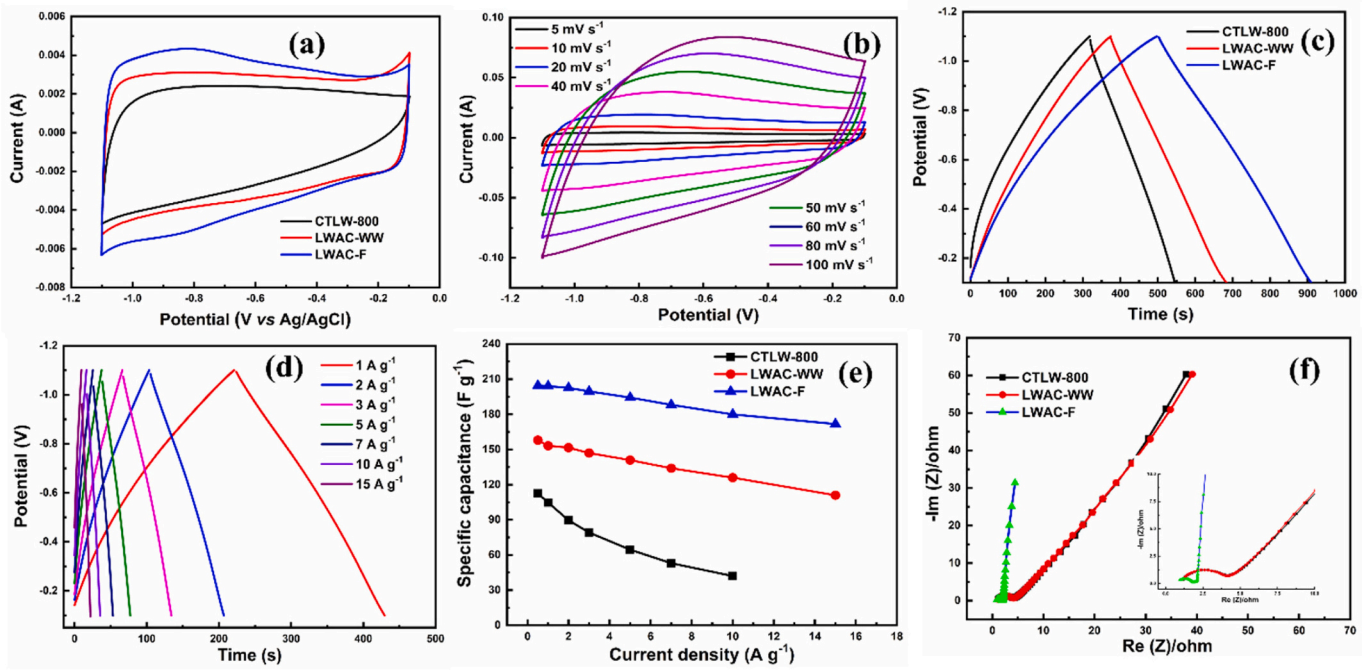

Fig. 8. Three electrode performance in 6 M KOH electrolyte, (a) CV performance of the electrodes, CTLW, LWAC-WW, and LWAC-F at 5 mV s^{-1} scan rate, (b) CV performance of the LWAC-F electrode at various scan rates, (c) CD curve for the prepared electrodes at 0.5 A g^{-1} current density, (d) CD performance of the LWAC-F electrode at extended current densities, (e) rate capability performance the electrodes at various current density, and (f) Nyquist plot with in the frequency range 500 kHz to 1 mHz (inset high frequency region of the Nyquist plot).

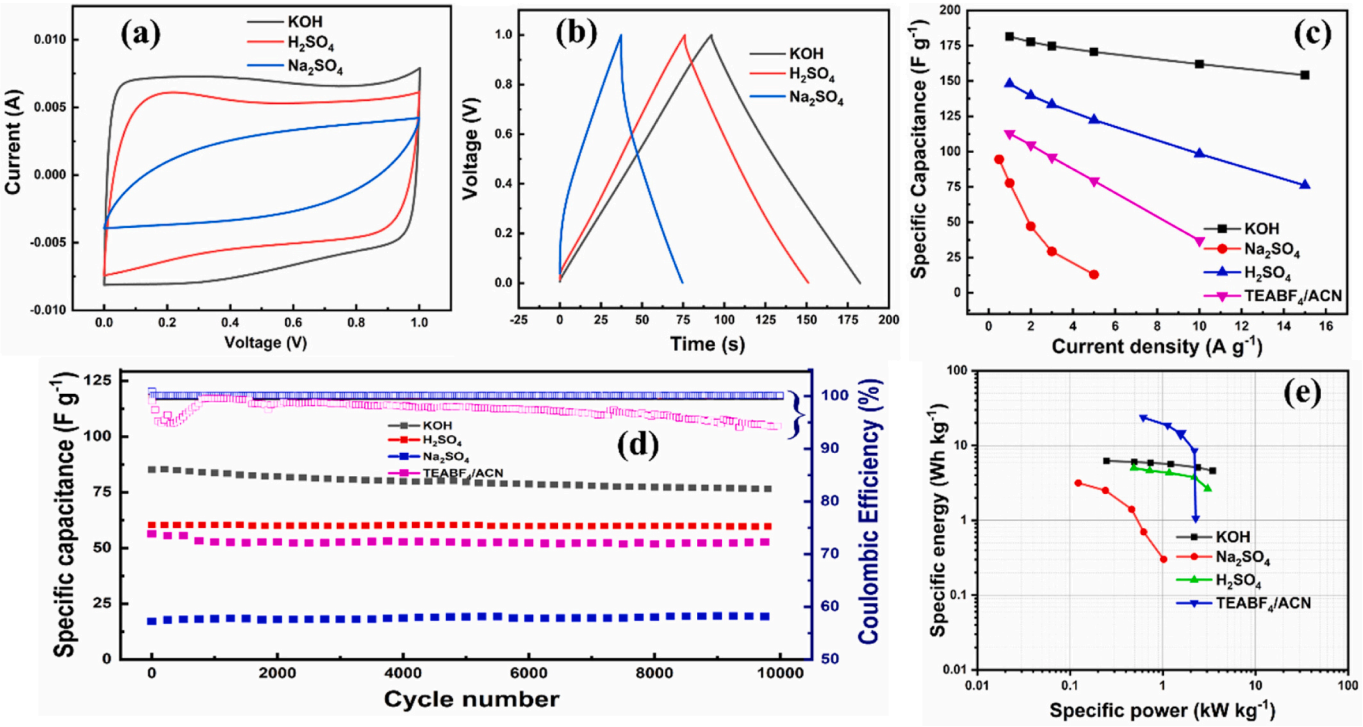

Fig. 9. Symmetric cell performance in various electrolytes, (a)&(b) comparative CV and GCD performance of the symmetric cell at 20 mV s^{-1} scan rate and 1 A g^{-1} current density, respectively, (c) rate performance of the LWAC-F cell, (d) cycle stability and coulombic efficiency of the cell at 3 A g^{-1} current density, (e) energy density and power density plot.

maintains 85% of its initial capacitance even at an elevated current density of 15 A g^{-1}.

Factors including ionic conductivity and the hydration sphere radius of the electrolyte directly influence the rate performance of the cell. The significant variation in performance, encompassing cell capacitance and rate in the KOH electrolyte, is ascribed to the superior conductivity and ionic mobility of K^+ and OH^- ions in contrast to SO_4^{2-} ions. In the H_2SO_4 electrolyte, despite the H^+ ion exhibiting a greater molar ionic

conductivity compared to K^+ ions, the rate and capacitance are constrained by the larger hydration sphere radii. Additionally, the ionic mobility of SO_4^{2} ions restricts their penetration into the porous structure of the LWAC-F. The poor performance of the cell in the Na_2SO_4 electrolyte is due to the lower molar ionic conductivity of Na^+ compared to K^+ and H^+ ions, higher hydration sphere radii, and lower ionic conductivity of SO_4^{2-} ions within the electrolyte. The rate performance of the supercapacitor in the organic electrolyte 1 M $TEABF_4$/ACN is limited due to the large ionic radii of the electrolyte ions, which restrict the accessibility of pores on the LWAC-F during high current charge-discharge cycles.

The cycle stability of the cell in different electrolytes was tested for 10,000 charge-discharge cycles at 3 A g^{-1}. The capacitance retention over cycle number and the corresponding coulombic efficiency are shown in Fig. 9(d). Here, the performance of the cell in 6 M KOH is reduced to 89.5% (99.9% efficiency) after 10,000 cycles compared to 95.7% (100% efficiency) in acidic and 112.6% (100% efficiency) in neutral electrolyte. There are several reasons for the decrease in specific capacitance of the supercapacitor in both aqueous and organic electrolytes. The pH of the electrolyte is a crucial factor; in acidic and alkaline electrolytes, the risk of electrode material corrosion during continuous charge-discharge cycles will reduce capacitance retention. Here, the highly concentrated alkaline electrolyte accelerates electrode corrosion and surface functional group breakdown. The rise in the specific capacitance in Na_2SO_4 with cycling results from the activation of pores or improved wettability of the electrode material. The excellent cycle stability of the cell in 1 M H_2SO_4 depends on the electrolyte concentration and conductivity. In the organic electrolyte, 1 M $TEABF_4$/ACN, the cell retains 93.2% of its capacitance after 10,000 cycles with 94.2% coulombic efficiency. The decrease in capacitance and efficiency results from the oxidation of acetonitrile and the formation of a passivation layer on the electrode surface. This reduces the effective surface area and blocks pore accessibility, leading to performance degradation. Despite the minimal decline, LWAC-F demonstrates good stability during 10,000 cycles of high current cycling. This is due to its fine microporous structure by chemical activation and high purity after the removal of Cr and other inorganic residues. Table S4 compares the electrochemical performance of the bio-waste-derived carbon reported previously with the current work. The Ragone plot of the LWAC symmetric cell is provided in Fig. 9(e). The cell delivers the maximum energy densities of 6.4 Wh kg^{-1} and 5.0 Wh kg^{-1} with 0.3 kW kg^{-1} and 0.25 kW kg^{-1} power densities in 6 M KOH and 1 M H_2SO_4 electrolyte at 1 A g^{-1}, respectively. The cell exhibits a high energy density of 23.7 Wh kg^{-1} with 0.6 kW kg^{-1} power density in the organic electrolyte. Energy density of the cell in the aqueous electrolyte lags that of the $TEABF_4$/ACN electrolyte due to the operating voltage limitations.

3.4. High-voltage Li-ion battery cathode application

The prepared $LiMnCrO_4$ cathode material was tested using a Li-metal reference/counter electrode in a coin cell format, with an upper cutoff voltage of 4.95 V. Typically, Cr-substituted spinels exhibit semiconductor properties, and the energy required for charge transfer tends to increase with higher Cr content in the $LiMnCrO_4$ structure. [43] The synthesized $LiMnCrO_4$ cathode material exhibits a Mn: Cr ratio of 1:1. The lithium extraction and insertion properties of the cathode half-cell were tested within two distinct voltage ranges, from 2.0 to 4.95 V and 3.5 to 4.95 V. The experiments were carried out using a BASE (1 M $LiPF_6$ in PC) and a modified electrolyte using 1 wt% LiDFOB electrolyte additive. The first five charge-discharge cycles of the cathode half-cell in LiDFOB modified electrolyte within the voltage range of 2 to 4.95 V are shown in Fig. 10(a). In the charge-discharge curve, a small voltage plateau around 4.0 V is associated with the Mn^{3+}/Mn^{4+} redox process involving the insertion and extraction of Li^+ ions into the 8a tetrahedral site. [43,44] The wide plateau region above 4.8 V is the Cr^{3+} to Cr^{4+} and a few Cr^{4+} to Cr^{6+} redox reactions associated with the three electron transfers. [45] A wide charge-discharge plateau appears below 3.0 V due to the reduction of Mn^{4+} to Mn^{3+}, involving Li-ion insertion into the 16c octahedral site of the spinel structure. [44,46] The discharge specific capacity from the first cycle for the $LiMnCrO_4$ cathode at 0.1C in LiDFOB modified electrolyte within the potential window of 2.0–4.95 V is 192.7 mAh g^{-1}, with an efficiency of 67.8%. The significant reduction in

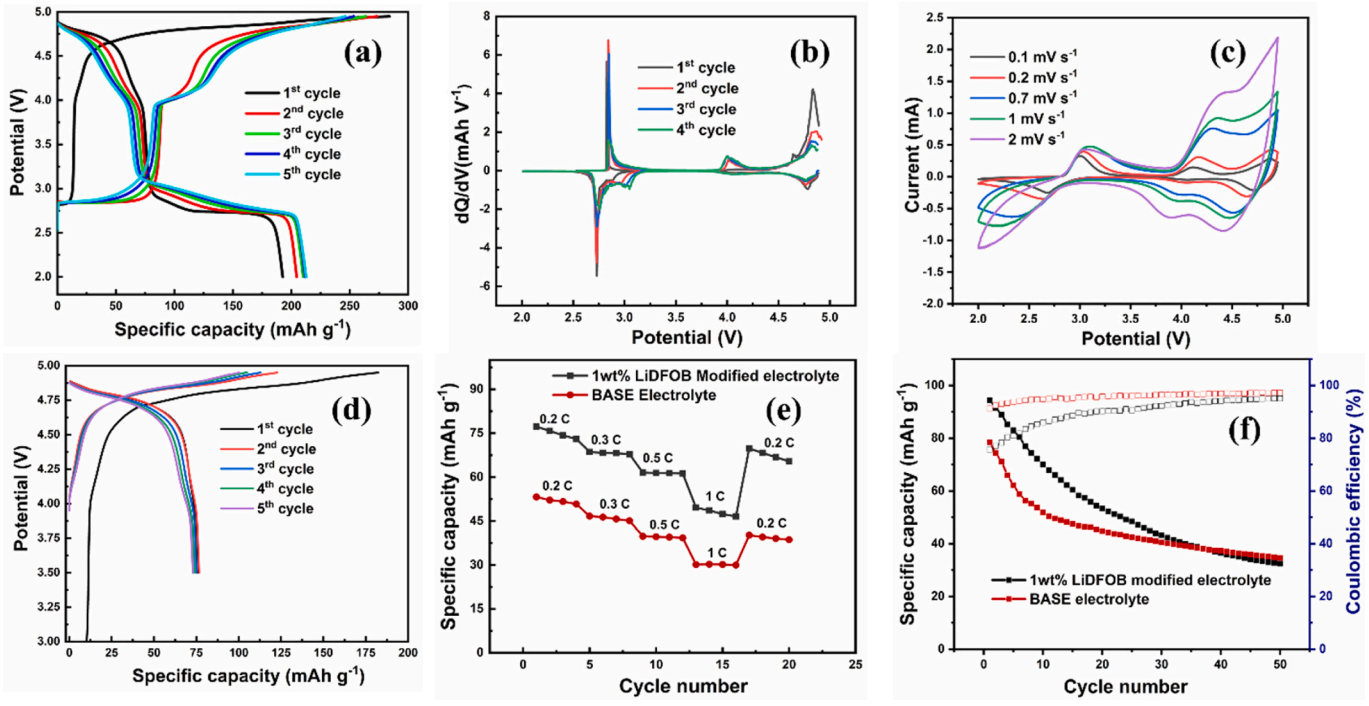

Fig. 10. (a) Charge-discharge curve of first 5 cycles of the $LiMnCrO_4$ cathode at 0.1C, (b) differential capacity for first 4 cycles, (c) CV profile at different scan rates, (d) charge-discharge curve of first 5 cycles in the voltage window 3.5 to 4.95 V, (e) rate capability performance and (f) cycle stability and efficiency at 0.2C for the half-cell in BASE and LiDFOB electrolytes.

efficiency and the variations in charging and discharging capacities are due to the irreversible side reactions occurring during the initial charging at 4.95 V. Earlier investigations using XPS reveal that charging-discharging in the $LiMnCrO_4$ cathode material beyond 4.88 V results in an irreversible change to Cr^{6+} and Mn^{3+} states, subsequently leading to the creation of defect or interface oxygen states. [47,48] This irreversible transformation of Cr and Mn will decrease the capacity of the cathode material. The differential capacity (dQ/dV) of the cathode half-cell within the potential window of 2.0 to 4.95 V during the first three cycles is shown in Fig. 10(b). The positive scan of the $LiMnCrO_4$ electrode reveals three main peaks that align with the charge-discharge curve. The intensity of the peaks at 4.75 V drops sharply after three cycles, indicating that cell operation above this potential causes a partially irreversible conversion of Cr^{3+} to Cr^{6+}. This Cr^{3+} to Cr^{6+} conversion disrupts the charge balance in the spinels, and to maintain electroneutrality, more Mn^{4+} is converted to Mn^{3+}. [49] Hence, the peak observed at 4.0 V, which corresponds to this Mn reduction, increases with cycling. Fig. 10(c) displays the cyclic voltammograms for the $LiMnCrO_4$ cathodes recorded at different scan rates from 0.1 to 2 mV s^{-1}. The CV diagram shows distinct peaks corresponding to the $LiMnCrO_4$//Li redox at their respective potentials. During the higher scan rate, there is a notable loss in the redox behavior of the cathode material. Fig. 10(d) displays the first five charge-discharge cycles of the half-cell within the potential window of 3.5 to 4.95 V using the LiDFOB-modified electrolyte. The initial discharge capacity of the half-cell is reduced to 76.7 mAh g^{-1} with 41.4% efficiency. Over half the capacity is lost in this voltage window because the major capacity contribution comes from the Mn^{3+}/Mn^{4+} redox below 3.0 V. The lower potential capacity of the cathode material limits its use in full cells due to the low energy resulting from the small cell voltage. Therefore, we chose a voltage range of 3.5 to 4.95 V for further rate capability and cycle stability tests. Fig. 10(e) shows the charge-discharge and rate performance of the half-cell with different C rates from 0.2 to 1C in the BASE and LiDFOB-modified electrolyte. We observed a capacity loss of 8.9 mAh g^{-1} from 0.2 to 0.3C and an overall capacity loss of 27.2 mAh g^{-1} when the C rate increased to 1C from 0.2C, which accounts for 35.5% of the total capacity lost. This high-capacity loss is mainly due to the structural changes linked to the spinel $LiMnCrO_4$ material and the formation of an electrochemically inactive secondary phase. Charging the $LiMnCrO_4$ cathode above 4.88 V causes the formation of an inactive surface phase and impedes Li diffusion into the remaining active phase. The cycle stability and coulombic efficiency of the half-cell were tested over 50 cycles, and the results are shown in Fig. 10(f). In the first 25 cycles, the capacity loss is significant in the LiDFOB modified electrolyte, maintaining only 48.9% of the initial capacity. In contrast, the cathode material retains 54% of its capacity in BASE electrolytes after 25 cycles. During the next 25 cycles, capacity retention drops to 32.6% for the LiDFOB modified cell and 43% of the initial capacity in the BASE electrolyte. The significant capacity loss during initial cycling mainly results from chemical and structural changes related to Cr and Mn conversion during high-voltage operation. More effort should be put into the development of high-voltage electrolytes and the modification of $LiMnCrO_4$ to improve the cell performance based on the $LiMnCrO_4$ cathode. Meanwhile, the application of recycled Cr from CTLW for other energy storage could be studied as well.

4. Conclusion

This present work details the preparation of activated carbon and Cr_2O_3 from chromium-tanned leather waste. Three distinct techniques, acid hydrolysis, physical separation, and alkaline hydrolysis, were employed to extract chromium from the carbonized leather waste. The extraction process efficiency was validated through various physico-chemical analyses. The activated carbon, after removing the inorganic residues, including Cr, was used as an electrode material for a symmetric supercapacitor. The prepared supercapacitor shows a high specific capacitance of 181.4 F g^{-1} at 1 A g^{-1} in 6 M KOH electrolyte. The operating window of the cell is extended to 2.7 V using 1 M $TEABF_4$/ACN organic electrolyte, and it shows a high energy density of 23.7 Wh kg^{-1} and a power density of 0.6 kW kg^{-1}. The recycled Cr_2O_3 derived from leather waste does not contain any impurities, enhancing its potential reuse in a range of applications. This Cr_2O_3 is used for the preparation of the $LiMnCrO_4$ cathode material, and the Li-ion half-cell tested using 1 wt% LiDFOB in 1 M $LiPF_6$/PC electrolyte shows a high specific capacity of 192.7 mAh g^{-1} in the voltage window 2–4.95 V. Hence, this works provided a sustainable, low-cost recycling method for Cr-tanned leather waste and its potential, but not limited to, futuristic applications.

CRediT authorship contribution statement

Nikhitha Joseph: Writing – original draft, Visualization, Methodology, Investigation, Conceptualization. **Tomáš Sáha:** Investigation. **Matej Micusik:** Investigation. **Petr Sáha:** Writing – review & editing, Supervision. **Haojie Fei:** Writing – review & editing, Visualization, Methodology, Investigation, Conceptualization.

Declaration of competing interest

The authors declare that there are no known competing financial interests or personal relationships that could have appeared to influence the work reported in this paper.

Acknowledgments

This work was supported by Horizon Europe (Grant No. 101078935) and the Technology Agency of the Czech Republic (TK03030157). N.J. acknowledges support within the “Creativity, Intelligence & Talent for the Zlín Region” (CIT- ZK) Program 2025. This work was supported by the Ministry of Education, Youth and Sports of the Czech Republic within the framework of the program DKRVO (RP/CPS/2024-28/005).

Appendix A. Supplementary data

Supplementary data to this article can be found online at https://doi.org/10.1016/j.est.2026.120397.

Data availability

Data will be made available on request.

References

[1] A.D. Covington, Modern tanning chemistry, Chem. Soc. Rev. 26 (1997) 111–126, https://doi.org/10.1039/CS9972600111.
[2] J. Jimenez-Paz, J.J. Lozada-Castro, E. Lester, O. Williams, L. Stevens, J. Barraza-Burgos, Solutions to hazardous wastes issues in the leather industry: Adsorption of chromium iii and vi from leather industry wastewaters using activated carbons produced from leather industry solid wastes, J. Environ. Chem. Eng. 11 (2023) 109715, https://doi.org/10.1016/j.jece.2023.109715.
[3] J. Kanagaraj, R.C. Panda, M.V. Kumar, Trends and advancements in sustainable leather processing: Future directions and challenges—A review, J. Environ. Chem. Eng. 8 (2020) 104379, https://doi.org/10.1016/j.jece.2020.104379.
[4] C.A. Bizzi, R.C. Zanatta, D. Santos, K. Giacobe, R.M. Dallago, P.A. Mello, E.M. M. Flores, Ultrasound-assisted extraction of chromium from residual tanned leather: An innovative strategy for the reuse of waste in tanning industry, Ultrason. Sonochem. 64 (2020) 104682, https://doi.org/10.1016/j.ultsonch.2019.104682.
[5] S. Ferraris, F. Gamna, T. Luxbacher, G. Maculotti, L. Giorio, J. Kholkhujaev, G. Genta, M. Galetto, A. Sarnataro, M. Nogarole, C. Florio, Comparative characterization of leather from different tanning processes as a contribution for a sustainable development of the leather industry, Sci. Rep. 15 (2025) 10608, https://doi.org/10.1038/s41598-025-94531-y.
[6] B. Lyu, R. Chang, D. Gao, J. Ma, Chromium footprint reduction: Nanocomposites as efficient Pretanning agents for cowhide shoe upper leather, ACS Sustain. Chem. Eng. 6 (2018) 5413–5423, https://doi.org/10.1021/acssuschemeng.8b00233.
[7] M. Vidaurre-Arbizu, S. Pérez-Bou, A. Zuazua-Ros, C. Martín-Gómez, From the leather industry to building sector: Exploration of potential applications of

discarded solid wastes, J. Clean. Prod. 291 (2021) 125960, https://doi.org/10.1016/j.jclepro.2021.125960.
[8] H. Long, X. Huang, Y. Liao, J. Ding, Recovery of Cr (VI) from tannery sludge and chrome-tanned leather shavings by Na2CO3 segmented calcination, J. Environ. Chem. Eng. 9 (2021) 105026, https://doi.org/10.1016/j.jece.2021.105026.
[9] X. Dang, H. Qiu, S. Qu, S. Liang, L. Feng, X. Wang, B-Cyclodextrin-based chrome-free tanning agent results in the sustainable and cleaner production of eco-leather, ACS Sustain. Chem. Eng. 12 (2024) 3715–3725, https://doi.org/10.1021/acssuschemeng.3c07446.
[10] M.A. Hashem, M.S. Nur-A-Tomal, Tannery solid waste valorization through composite fabrication: A waste-to-wealth approach, environ Prog sustain, Energy 37 (2018) 1722–1726, https://doi.org/10.1002/ep.12860.
[11] C.E. Aguilar Quiroz, Y. Guevara Ruiz, J.F. Urquiaga Rios, E.G. Layza Escobar, M. A. Siqueira Rodrigues, Electrochemical separation of chromium/collagen from wet blue in a single step: Recycling of tannery waste to promote a circular economy, Results Eng. 26 (2025) 104828, https://doi.org/10.1016/j.rineng.2025.104828.
[12] V. Muralidharan, S. Palanivel, M. Balaraman, Turning problem into possibility: A comprehensive review on leather solid waste intra-valorization attempts for leather processing, J. Clean. Prod. 367 (2022) 133021, https://doi.org/10.1016/j.jclepro.2022.133021.
[13] C.R. China, M.M. Maguta, S.S. Nyandoro, A. Hilonga, S.V. Kanth, K.N. Njau, Alternative tanning technologies and their suitability in curbing environmental pollution from the leather industry: A comprehensive review, Chemosphere 254 (2020) 126804, https://doi.org/10.1016/j.chemosphere.2020.126804.
[14] C. Mu, W. Lin, M. Zhang, Q. Zhu, Towards zero discharge of chromium-containing leather waste through improved alkali hydrolysis, Waste Mgt 23 (2003) 835–843, https://doi.org/10.1016/S0956-053X(03)00040-0.
[15] J.C. Beltrán-Prieto, R. Veloz-Rodríguez, M.C. Pérez-Pérez, J.L. Navarrete-Bolaños, E. Vázquez-Nava, H. Jiménez-Islas, J.E. Botello-Álvarez, Chromium recovery from solid leather waste by chemical treatment and optimisation by response surface methodology, Chem. Ecol. 28 (2012) 89–102, https://doi.org/10.1080/02757540.2011.628016.
[16] L. Swierczek, P. Hercel, I. Konkol, K. Kuligowski, A. Cenian, Chromium substitution extraction method for its recovery from chromium-tanned leather waste, Materials 18 (2024) 118, https://doi.org/10.3390/ma18010118.
[17] A.S. Popiolski, R.M. Dallago, J. Steffens, M.L. Mignoni, L.D. Venquiaruto, D. Santos, F.A. Duarte, Ultrasound-assisted extraction of Cr from residual tannery leather: Feasibility of ethylenediaminetetraacetic acid as the extraction solution, ACS Omega 3 (2018) 16074–16080, https://doi.org/10.1021/acsomega.8b02241.
[18] J.A. Arcibar-Orozco, A. Saldaña-Robles, R. Rangel-Méndez, L. Nielsen, H. Baltazar-Campos, E.A. Garduño-Cruces, B.V. Hernandez-López, F. Caballero-Briones, Revalorization of chromium-tanned leather shavings into carbon materials and re-tanning solution, Biomass Convers. Biorefinery 14 (2024) 17913–17925, https://doi.org/10.1007/s13399-023-04014-1.
[19] M. Erdem, Chromium recovery from chrome shaving generated in tanning process, J. Hazard. Mater. 129 (2006) 143–146, https://doi.org/10.1016/j.jhazmat.2005.08.021.
[20] D.C. Martínez-Casillas, I.L. Alonso-Lemus, I. Mascorro-Gutiérrez, A.K. Cuentas-Gallegos, Leather waste-derived biochar with high performance for supercapacitors, J. Electrochem. Soc. 165 (2018) A2061–A2068, https://doi.org/10.1149/2.0421810jes.
[21] P.R. de Oliveira, C. Kalinke, J.L. Gogola, A.S. Mangrich, L.H.M. Junior, M. F. Bergamini, The use of activated biochar for development of a sensitive electrochemical sensor for determination of methyl parathion, J. Electroanal. Chem. 799 (2017) 602–608, https://doi.org/10.1016/j.jelechem.2017.06.020.
[22] L.C. Oliveira, C.V. Coura, I.R. Guimaraes, M. Goncalves, Removal of organic dyes using Cr-containing activated carbon prepared from leather waste, J. Hazard. Mater. 192 (2011) 1094–1099, https://doi.org/10.1016/j.jhazmat.2011.06.014.
[23] Q. Han, L. Chen, X. Wang, R. Sun, J. Li, X. Guan, Optimizing waste utilization value: Fabrication of multi-functional high-performance electrocatalysts via in situ chemical transformation on chromium-tanned collagen fibers, J. Environ. Chem. Eng. 12 (2024) 114886, https://doi.org/10.1016/j.jece.2024.114886.
[24] N. Roshini, K. Patchai Murugan, K. Sekar, T.S. Natarajan, Bismuth oxyhalides-chrome tanned leather shaving waste activated carbon nanocomposites: Evaluating the influence of halides and chromium oxide-embedded activated carbon on catalytic activity, J. Environ. Chem. Eng. 13 (2025) 115089, https://doi.org/10.1016/j.jece.2024.115089.
[25] J.A. Arcibar-Orozco, B.S. Barajas-Elías, H. Baltazar-Campos, R. Rangel-Mendez, Preparation of carbon materials from chromium-tanned leather shavings for the removal of dyes from aqueous solution, Appl Water Sci 12 (2022) 213, https://doi.org/10.1007/s13201-022-01734-z.
[26] N. Konikkara, L.J. Kennedy, J.J. Vijaya, Preparation and characterization of hierarchical porous carbons derived from solid leather waste for supercapacitor applications, J. Hazard. Mater. 318 (2016) 173–185, https://doi.org/10.1016/j.jhazmat.2016.06.037.
[27] F. Ma, S. Ding, H. Ren, P. Peng, Preparation of chrome-tanned leather shaving-based hierarchical porous carbon and its capacitance properties, RSC Adv. 9 (2019) 18333–18343, https://doi.org/10.1039/c9ra03139a.
[28] N. Konikkara, N. Punithavelan, L.J. Kennedy, J.J. Vijaya, A new approach to solid waste management: Fabrication of supercapacitor electrodes from solid leather wastes using aqueous KOH electrolyte, clean Techn environ, Policy 19 (2016) 1087–1098, https://doi.org/10.1007/s10098-016-1301-1.
[29] P.-A. Carolina, R.-R. Roberto, O.-S. Miguel, S.G.-G. David, R.-M. Rene, F.C.-R. Luis, A.-B. Miguel, A.A.-O. Javier, N-doped activated carbons from leather waste produced by microwave activation for use as the cathode of Li-S batteries, New Carbon Mater 40 (2025) 382–395, https://doi.org/10.1016/S1872-5805(25)60958-9.
[30] J. Sun, X. Tian, C. Xu, H. Chen, Porous CuCo2O4 microtubes as a promising battery-type electrode material for high-performance hybrid supercapacitors, J. Mater. 7 (2021) 1358–1368, https://doi.org/10.1016/j.jmat.2021.03.011.
[31] H. Sun, Y. Miao, G. Wang, X. Han, C. Xu, J. Zhu, H. Chen, Battery-type ZnCo2O4 nanosheets and nanowires as advanced cathode materials for hybrid supercapacitors with ultra-long cycling stability, J. Energy Storage 92 (2024) 112189, https://doi.org/10.1016/j.est.2024.112189.
[32] H. Chen, F. Tian, X. Han, H. Sun, G. Wang, Z. Zhang, J. Zhu, C. Xu, Porous MnCo2O4 nanoplatelets and nanoflowers as cathode materials for high-performance asymmetric supercapacitor application, J. Energy Storage 112 (2025) 115587, https://doi.org/10.1016/j.est.2025.115587.
[33] M. Velusamy, B. Chakali, S. Ganesan, F. Tinwala, S. Shanmugham Venkatachalam, Investigation on pyrolysis and incineration of chrome-tanned solid waste from tanneries for effective treatment and disposal: An experimental study, Environ. Sci. Pollut. Res. 27 (2020) 29778–29790, https://doi.org/10.1007/s11356-019-07025-6.
[34] M. Sathish, K.J. Sreeram, J. Raghava Rao, B. Unni Nair, Cyclic carbonate: A recyclable medium for zero discharge tanning, ACS Sustain. Chem. Eng. 4 (2016) 1032–1040, https://doi.org/10.1021/acssuschemeng.5b01121.
[35] R. Sinha, R. Kumar, P. Sharma, N. Kant, J. Sharma, T.M. Aminabhavi, Removal of hexavalent chromium via biochar-based adsorbents: State-of-the-art, challenges, and future perspectives, J. Environ. Manag. 317 (2022) 115356, https://doi.org/10.1016/j.jenvman.2022.115356.
[36] C.R. Alves, P.J.W.K.d. Buzin, N.C. Heck, I.A.H. Schneider, Utilization of ashes obtained from leather shaving incineration as a source of chromium for the production of HC-FeCr alloy, Miner. Eng. 29 (2012) 124–126, https://doi.org/10.1016/j.mineng.2011.12.009.
[37] L. Wang, J. Li, Y. Jin, M. Chen, J. Luo, X. Zhu, Y. Zhang, Study on the removal of chromium(III) from leather waste by a two-step method, J. Ind. Eng. Chem. 79 (2019) 172–180, https://doi.org/10.1016/j.jiec.2019.06.030.
[38] K. Fela, K. Wieczorek-Ciurowa, M. Konopka, Z. Wozny, Present and prospective leather industry waste disposal, Pol. J. Chem. Technol. 13 (2011) 53–55, https://doi.org/10.2478/v10026-011-0037-2.
[39] K.-S. Kim, S.-W. Lee, H.-S. Moon, H.-J. Kim, B.-W. Cho, W.-I. Cho, J.-B. Choi, J.-W. Park, Electrochemical properties of Li–Cr–Mn–O cathode materials for lithium secondary batteries, J. Power Sources 129 (2004) 319–323, https://doi.org/10.1016/j.jpowsour.2003.11.027.
[40] A. Kitajou, S. Matsuda, K. Ohara, K. Ikeda, S. Muto, Cathode properties of a controlled crystallinity nano-$Li_{1.2}Cr_{0.4}Mn_{0.4}O_2$ cathode for lithium ion batteries, RSC Mechanochem 2 (2025) 54–60, https://doi.org/10.1039/d4mr00051j.
[41] X. Li, D. Li, D. Song, X. Shi, X. Tang, H. Zhang, L. Zhang, Unravelling the structure and electrochemical performance of Li-Cr-Mn-O cathodes: From spinel to layered, ACS Appl. Mater. Interfaces 10 (2018) 8827–8835, https://doi.org/10.1021/acsami.7b18097.
[42] J. Stejskal, H. Fei, J. Vilčáková, N. Joseph, P. Sáha, T. Sáha, B. Grycová, K. Klemencová, P. Lestinsky, M. Trchová, J. Prokeš, Using tanned leather waste to derive biochars for supercapacitor electrodes in various electrolytes, Biomass Convers. Biorefinery 15 (2025) 17251–17265, https://doi.org/10.1007/s13399-024-06348-w.
[43] T.A. Arunkumar, A. Manthiram, Influence of chromium doping on the electrochemical performance of the 5V spinel cathode $LiMn_{1.5}Ni_{0.5}O_4$, Electrochem. Acta 50 (2005) 5568–5572, https://doi.org/10.1016/j.electacta.2005.03.033.
[44] E.-S. Lee, K.-W. Nam, E. Hu, A. Manthiram, Influence of Cation Ordering and Lattice Distortion on the Charge–Discharge Behavior of $LiMn_{1.5}Ni_{0.5}O_4$ Spinel between 5.0 and 2.0 V, Chem. Mater. 24 (2012) 3610–3620, https://doi.org/10.1021/cm3020836.
[45] Z. Lu, J.R. Dahn, Structure and Electrochemistry of Layered Structure and Electrochemistry of Layered $Li[CrLi_{(1/3-x/3)}Mn_{(2/3-2/3)}]O_2$, J. Electrochem. Soc. 149 (2002) A1454, https://doi.org/10.1149/1.1513557.
[46] E.-S. Lee, A. Huq, H.-Y. Chang, A. Manthiram, High-voltage, high-energy layered-spinel composite cathodes with superior cycle life for Lithium-ion batteries, Chem. Mater. 24 (2012) 600–612, https://doi.org/10.1021/cm2034992.
[47] S. Oswald, K. Nikolowski, H. Ehrenberg, XPS investigations of valence changes during cycling of $LiCrMnO_4$-based cathodes in Li-ion batteries, Surf. Interface Anal. 42 (2010) 916–921, https://doi.org/10.1002/sia.3296.
[48] E. Lee, J.S. Park, T. Wu, C.-J. Sun, H. Kim, P.C. Stair, J. Lu, D. Zhou, C.S. Johnson, Role of Cr^{3+}/Cr^{6+} redox in chromium-substituted $Li_2MnO_3{\cdot}LiNi_{1/2}Mn_{1/2}O_2$ layered composite cathodes: Electrochemistry and voltage fade, J. Mater. Chem. A 3 (2015) 9915–9924, https://doi.org/10.1039/c5ta01214g.
[49] E. Iwata, K.-i. Takahashi, K. Maeda, T. Mouri, Capacity failure on cycling or storage of lithium-ion batteries with Li–Mn–O ternary phases having spinel-framework structure and its possible solution, J. Power Sources 81-82 (1999) 430–433, https://doi.org/10.1016/S0378-7753(99)00227-X.